**ADVANCED
SCIENCE NEWS**
www.advancedsciencenews.com

**ADVANCED
FUNCTIONAL
MATERIALS**
www.afm-journal.de

FULL PAPER

Atomic Layer Deposited Non-Noble Metal Oxide Catalyst for Sodium–Air Batteries: Tuning the Morphologies and Compositions of Discharge Product

Qian Sun, Jian Liu, Xia Li, Biqiong Wang, Hossein Yadegari, Andrew Lushington, Mohammad N. Banis, Yang Zhao, Wei Xiao, Ning Chen, Jian Wang, Tsun-Kong Sham, and Xueliang Sun*

Catalysts can play a critical role in the development of sodium–air batteries (SABs). Atomic layer deposition (ALD) technology enables rational design and atomic utilization of catalyst by homogenously distributing catalytically active material on a variety of substrates. Here, a novel hierarchical nanostructured Co_3O_4 is decorated on carbon nanotubes by ALD ($CNT@Co_3O_4$) and used as a catalyst for SABs. $CNT@Co_3O_4$ demonstrates better performance and longer cycle life than a mechanically mixed CNT/Co_3O_4 nanocomposite. Well-dispersed ALD Co_3O_4 catalyst on CNTs, which serves as functionalized active sites, enables rapid electron exchange and high oxygen reduction/evolution activities. Synchrotron-based X-ray analysis including X-ray absorption near edge structure, extended X-ray absorption fine structure, and scanning transmission X-ray microscopy characterization techniques have been employed to elucidate the activity of Co_3O_4 and to investigate the nanoscale discharge product distribution found in SABs. This analysis reveals that Co_3O_4 catalyst can promote the electrochemical decomposition of sodium peroxide, superoxide, and carbonates. The role of the catalyst in SABs is clarified and discussed in detail.

1. Introduction

Recently, Na-based energy storage and conversion devices are attracting increasing research interests due to their environmentally benign characteristics as well as the low cost and abundant resource of Na element.[1–6] Similar to Li–air batteries (LABs),[7–10] sodium–air batteries (SABs)[11–15] have been proposed to be an advanced battery system for the potential applications in future electric vehicles and hybrid electric vehicles. The theoretical energy density of SABs is calculated to be 1601 and 1101 Wh kg^{-1} corresponding to the formation of Na_2O_2[16–23] and NaO_2,[24–27] respectively, which are dramatically higher than those of conventional Li-ion batteries ($\approx$160 Wh kg^{-1}). Compared to LABs, SABs have a relatively lower theoretical energy density, but present greatly reduced charging overpotential,[24] resulting in a significantly improved energy utilization efficiency.

The oxygen reduction reaction (ORR) and oxygen evolution reaction (OER) are two critical processes that dominate the energy storage capabilities of LABs and SABs. The ORR consists of reducing absorbed oxygen on the surface of the air electrode as well as coupling oxygen to Li^+/Na^+, resulting in precipitated oxides. The OER reaction on the other hand is the reverse process of the ORR. The sluggish kinetics of the OER and ORR are associated with gas–liquid–solid three-phase reaction mechanism, resulting in a high overpotential and a low energy efficiency of metal–air batteries. In addition, the insulating nature of solid-state discharge products, which generally accumulate on the surface of the air electrode,[1–6] results in diminished electronic conductivity of the discharged air electrodes. Therefore, an efficient heterogeneous catalyst grown on conductive carbon substrates is expected to overcome the aforementioned obstacles in LABs and SABs. In addition, sodium superoxide (NaO_2) was observed to be a relatively stable component in the discharge products of SABs besides sodium peroxide (Na_2O_2). In contrast, Li_2O_2 is generally detected as the stable discharge product in LABs and LiO_2 is generally found to be an intermediate phase during ORR. Recently, Lu et al. reported that an Ir–reduced graphene oxide (RGO) catalyst can stabilize the formation of lithium superoxide LiO_2 as the discharge product in Li–O₂ battery.[28] Thus, the question remains of whether or not a catalyst can promote the formation/decomposition of superoxides. Revealing the role of catalysts in SABs is crucial to the understanding of alkali metal–air batteries.

Dr. Q. Sun, Dr. J. Liu, Dr. X. Li, B. Wang,
Dr. H. Yadegari, A. Lushington, Dr. M. N. Banis,
Y. Zhao, W. Xiao, Prof. X. Sun
Department of Mechanical and Materials Engineering
University of Western Ontario
London, Ontario N6A 5B9, Canada
E-mail: xsun@eng.uwo.ca
B. Wang, Prof. T.-K. Sham
Department of Chemistry
University of Western Ontario
London, Ontario N6A 5B7, Canada
Dr. N. Chen, Dr. J. Wang
Canadian Light Source
Saskatoon S7N 0X4, Canada

FULL PAPER

A rational design for catalysts used in SABs should employ the following factors: (1) a highly conductive and porous catalyst substrate, ensuring high electron conductivity and rapid liquid/gas transportation; (2) nanostructured catalyst particles to increase catalyst utilization; (3) abundant and well-dispersed catalyst sites to improve OER/ORR kinetics; (4) low cost and environmentally benign properties of the catalyst chemical composition. Therefore, a uniformly and highly dispersed catalyst embedded in a conductive carbon support is considered to be a reasonable choice as the air electrode for alkali metal–air batteries. Nonetheless, conventional fabrication routes (e.g., grinding and mechanical milling) have drawbacks of discrete distribution and poor adherence between the catalyst and the substrate as well as the possible destruction on the original porous structure of the substrates. In order to overcome these difficulties, atomic layer deposition (ALD) technique has been thus considered as a possible solution to fabricating efficient catalysts for LABs[29,30] and SABs.

ALD is a thin-film deposition technique based on sequential self-terminating reactions between gas phase reagents and a functionalized surface.[31,32] ALD proceeds with alternative introduction and removal of vapor precursors, during which saturated surface reactions take place. This unique reaction mechanism employed in ALD enables extremely uniform and conformal thin-film growth with nanoscale control over thickness on a variety of substrates. It is worthy to note that ALD is also especially applicable to 3D porous structures, which can seldom be uniformly coated by other gas phase deposition techniques. These merits make ALD an exceptional choice for the design and fabrication of functional catalysts.[33]

Lei et al. first demonstrated the ALD of Pd nanoparticles on a porous carbon support as a catalyst for LABs.[29] Later, they also reported the use of an ALD Al_2O_3 coating which was proved to improve the performance of the Pd catalyst by blocking defect sites on the surface of carbon.[30] Xie et al. reported the ALD of Ru nanoparticles on 3D nanostructured $TiSi_2$ substrate as a high performance catalyst for LABs.[34] Schroeder et al. also reported the ALD of Ru RuO_2 on multiwalled carbon nanotube sponge substrates as long life air electrodes for LABs.[35] Recently, our group has reported the ALD of stabilized Pt/ZrC and Pt/ZrO_2 electrocatalysts for ORR in fuel cells.[36,37] Nevertheless, these studies have mainly focused on noble metals as catalytic centers. In contrast, a non-noble metal-based catalyst should be even preferred for feasible practical applications considering its lower cost and richer elemental abundance. Thus, nanostructured cobalt oxides (CoO,[38,39] Co_3O_4,[40–44] and $La_{0.5}Sr_{0.5}CoO_{2.91}$[45]) have been developed as efficient catalysts for LABs. Meanwhile, there have been numerous studies reporting the ALD fabrication of cobalt oxide from different precursors.[46–53] However, to our best knowledge, there is still no report on the electrochemical behavior and performance of cobalt oxide or other ALD non-noble metal oxide catalyst for SABs.

In this work, we fabricated ALD Co_3O_4 decorated carbon nanotubes (CNT@Co_3O_4) and tested their electrochemical activity as an air electrode catalyst for SABs for the first time. For comparison, CNT/Co_3O_4 nanocomposite powders were also prepared by mechanically grinding Co_3O_4 nanoparticles with CNTs. The electrochemical performance of the air electrode

catalysts were investigated by charge and discharge cycling, cyclic voltammetry (CV), and electrochemical impedance spectroscopy (EIS) measurements. Their reaction mechanisms were studied by X-ray diffraction (XRD), Fourier-transform infrared spectroscopy (FT-IR), scanning electron microscopy (SEM), and energy-dispersive X-ray spectroscopy (EDX) characterizations. Additionally, synchrotron-based hard X-ray absorption spectroscopy (XAS) and soft X-ray scanning transmission X-ray microscopy (STXM) characterizations were also carried out to probe the activity of catalyst and nanoscale discharge product distribution in SABs for the first time. The role of catalyst in SABs is also discussed and clarified in detail.

2. Results and Discussion

2.1. Fabrication and Physical Characterization of the ALD CNT@Co_3O_4 and Mechanically Grinded CNT/Co_3O_4 Air Electrodes

2.1.1. Synthesis of ALD CNT@Co_3O_4 and Mechanically Mixed CNT/Co_3O_4 Nanocomposites

The fabrication process for ALD CNT@Co_3O_4 and mechanically grinded CNT/Co_3O_4 nanocomposite are schematically shown in **Figure 1**. Bis(cyclopentadienyl)cobalt(II) (CoCp$_2$) and O_2 were pulsed into the ALD chamber in a cyclic manner with a N$_2$ purge step between each pulse. The self-saturated reaction mechanism of the ALD process enables a layer-by-layer formation of Co_3O_4 on the CNT substrate to form CNT@Co_3O_4. The weight percentage of Co_3O_4 in CNT@Co_3O_4 is determined to be 15.39% by inductively coupled plasma atomic emission spectroscopy (ICP-AES). The calculation details can be found in the Supporting Information. In comparison, commercial Co_3O_4 nanoparticles were grinded with CNT powders in a weight ratio of 1:9 to make CNT/Co_3O_4. Afterward, both of the obtained CNT–Co_3O_4 nanocomposite powders are mixed with a polymer binder and dissolved in an organic solvent, and then drop-casted on a porous polymer separator to fabricate the air electrodes.
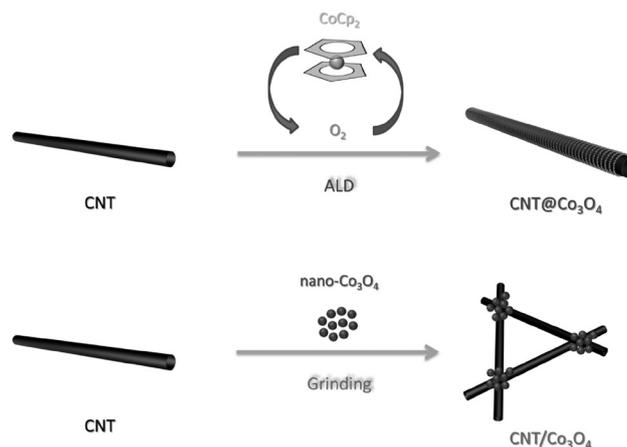

Figure 1. Schematic diagram of the fabrication of ALD CNT@Co_3O_4 and mechanically grinded CNT@Co_3O_4 nanocomposite.

2.1.2. Morphological and Structural Characterization

SEM images of $CNT@Co_3O_4$ and CNT/Co_3O_4 air electrodes are shown in **Figure 2**a,b,g,h, respectively. The air electrodes show a porous structure which were formed due to the stacking of the CNT skeleton units (Figure 2a,g). This spongy structure is permeable to the electrolyte and air supply, and is thus preferable for use in SABs. The higher resolution images reveal that nanoscale Co_3O_4 particles were evenly distributed on the surface of CNTs after the ALD process (Figure 2b). The formation of such discrete compound dots is often observed in the beginning period of ALD process,[29] mainly as a result of the initial nucleation process in ALD. In contrast, the mechanically grinded CNT/Co_3O_4 exhibited an uneven dispersion of Co_3O_4 on the CNTs, with Co_3O_4 nanoparticles aggregating between CNTs (Figure 2h). EDX mapping of the two prepared air electrodes provides a more direct evidence of the consistent and inconsistent cobalt oxide distribution by illustrating the element allocation (Figure 2c–f for $CNT@Co_3O_4$ and Figure 2i–l for CNT/Co_3O_4), supporting the above observation from the SEM. From the SEM and EDX results, it can be anticipated that the chemisorbed cobalt oxide prepared by ALD should demonstrate better electrical contact and exhibit an increased exposing area for OER compared to the sample fabricated via conventional grinding, and therefore be beneficial toward electrochemical performance in SABs. In addition, the XRD pattern of the ALD-coated CNT powder sample well matched the combination of the XRD patterns of pristine CNT and standard pattern from the Joint Committee on Powder Diffraction Standards (JCPDS) database (Figure 2m), confirming that the chemical composition of the resulted ALD cobalt oxide is Co_3O_4.

2.2. Electrochemical Characterization of the $CNT@Co_3O_4$ and CNT/Co_3O_4 Air Electrodes as Catalysts for Sodium–Air Batteries

2.2.1. Cell Configuration

To examine the electrochemical performance of the $CNT@Co_3O_4$ and CNT/Co_3O_4 air electrodes, Swagelok-type Na–air cells were used and tested in a sealed container under dried air.[54] In a representative Na–air cell, a metallic Na foil was used as an anode and a $CNT@Co_3O_4$ or CNT/Co_3O_4 air electrode was used as

Figure 2. Morphology and element distribution of a–f) ALD $CNT@Co_3O_4$ and g–l) CNT/Co_3O_4 nanocomposite by SEM and EDX mapping. m) XRD pattern of (1) pristine CNT and (2) ALD $CNT@Co_3O_4$; standard XRD pattern of Co_3O_4 from JCPDS database is also shown for comparison.

a cathode, with a polypropylene (PP)-based polymer separator in-between. $NaCF_3SO_3$/diethylene glycol dimethyl ether (DEGDME) was used as the electrolyte.[20,24,55] More details
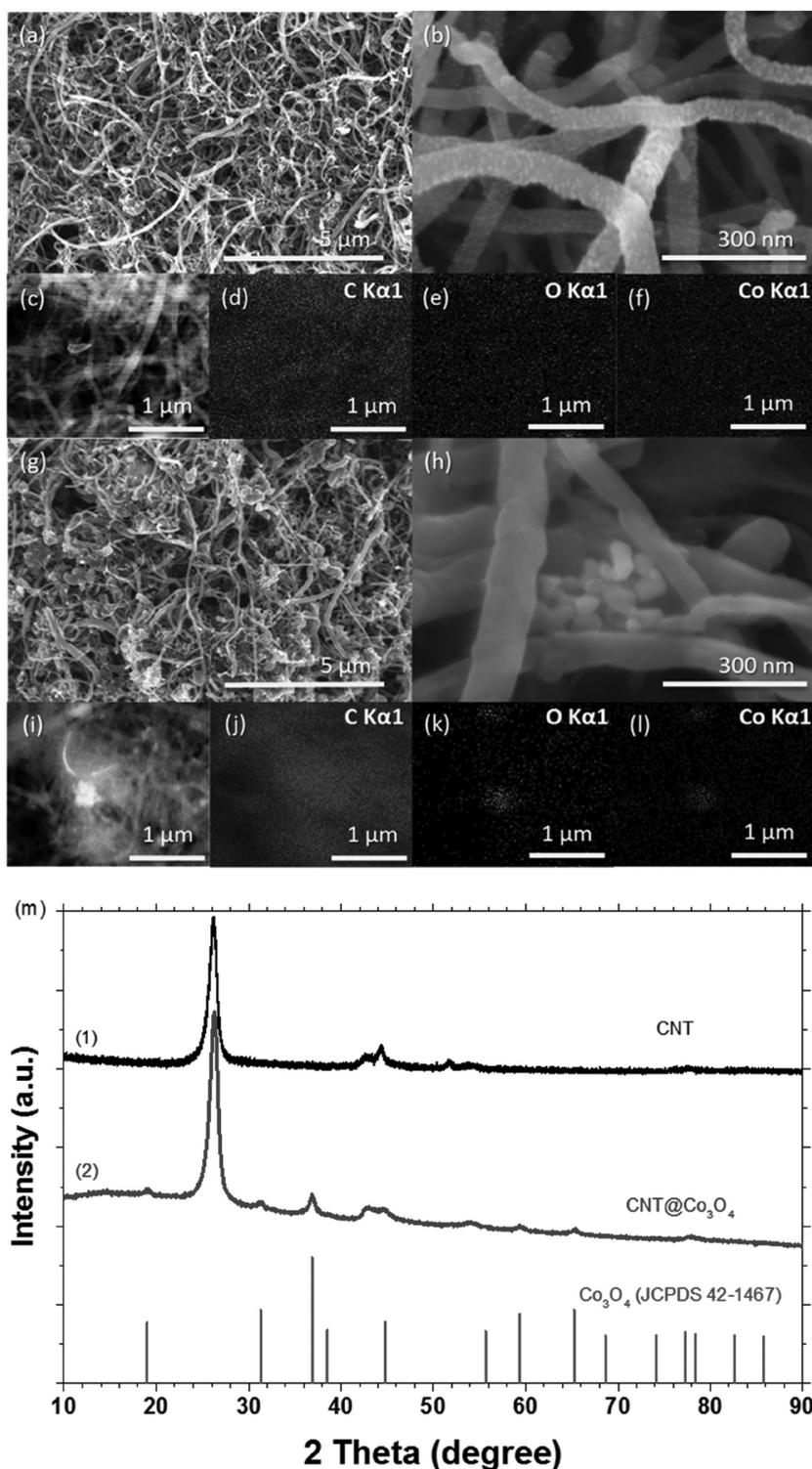
about the cell configuration are described in the Experimental Section.

2.2.2. Charge and Discharge Measurements

Figure 3a demonstrates the first charge and discharge curves of CNT@Co$_3$O$_4$, CNT/Co$_3$O$_4$, and pristine CNT air electrodes at a current density of 150 mA g^{-1}. The applied current densities and capacities are all calculated based on the total weight of CNT and cobalt oxide catalyst. All three air electrodes exhibit similar discharge curves. The discharge capacity of CNT@Co$_3$O$_4$ is slightly larger than that of pristine CNT, while the latter possesses a 15% higher value than that of the CNT/Co$_3$O$_4$ air

electrode. The decreased capacity of CNT/Co$_3$O$_4$ may be attributed to the poor electrical contact between cobalt oxide nanoparticles and the CNT substrate. Nazar and co-workers reported that a Co$_3$O$_4$ grown on reduced graphene oxide (Co$_3$O$_4$/RGO) electrode did not exhibit significant discharge capacity unless it was mixed with conductive carbon (Ketjenblack carbon black).[43] CNT@Co$_3$O$_4$ air electrode obtained by ALD, on the other hand, is benefited from the Ohmic contact between the CNT core and Co$_3$O$_4$ shell, which contributes to its improved performance. When focusing on the beginning stages of the charge and discharge behavior of all the three air electrodes (Figure 3b), it can be clearly found that the spike observed in the discharge curves of pristine CNT air electrode obviously alleviates or disappears in those of CNT/Co$_3$O$_4$ or CNT@Co$_3$O$_4$
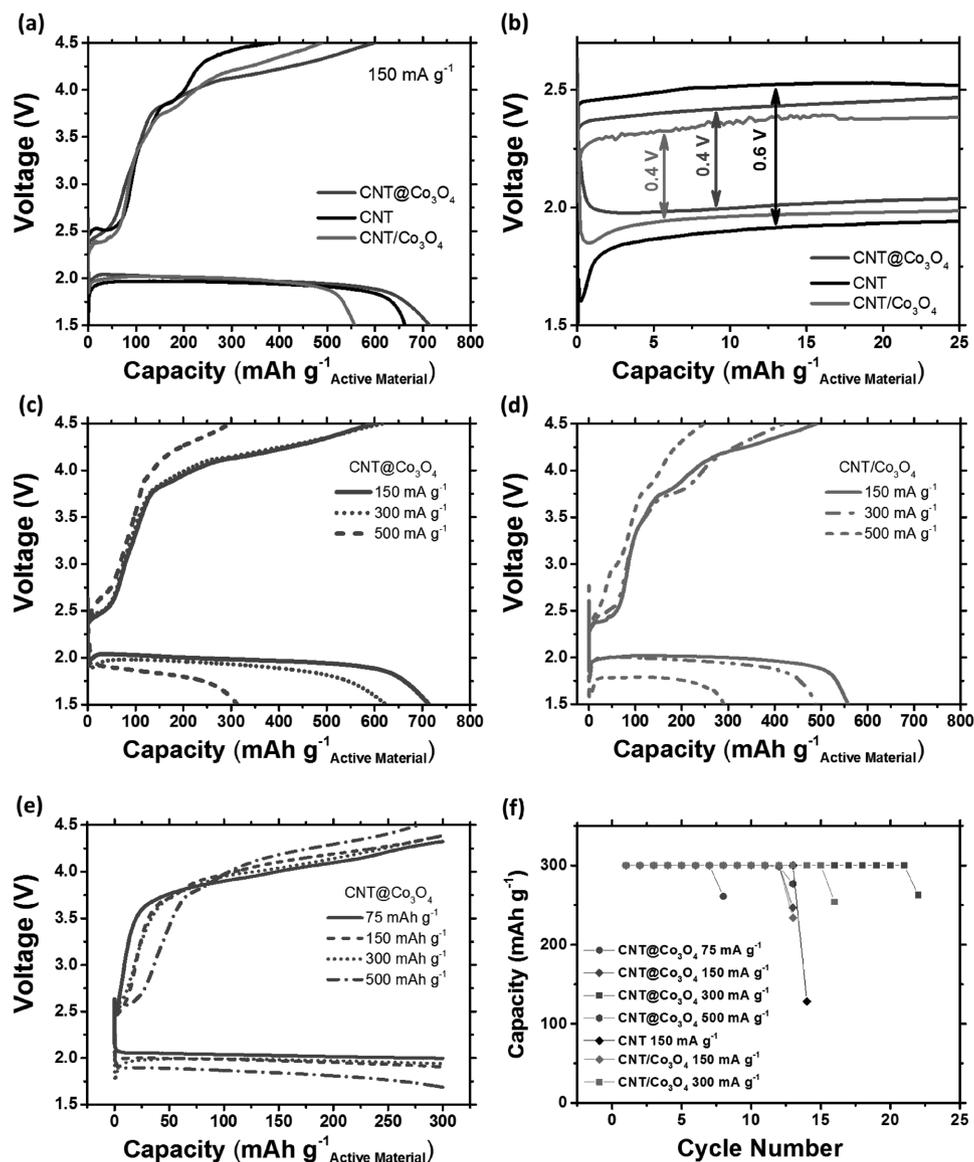

Figure 3. a,b) The comparison of charge and discharge profiles of SABs with ALD CNT@Co$_3$O$_4$, CNT/Co$_3$O$_4$ nanocomposite, and pristine CNT air electrodes at 150 mA g^{-1}. Charge and discharge profiles of SABs with c) ALD CNT@Co$_3$O$_4$ and d) CNT/Co$_3$O$_4$ nanocomposite air electrodes at the current densities of 150, 300, and 500 mA g^{-1}. e) Charge and discharge profiles of SABs with ALD CNT@Co$_3$O$_4$ air electrodes at the current densities of 150, 300, and 500 mA g^{-1} at the same cut-off capacity of 300 mAh g^{-1}. f) Cycling retention of SABs with ALD CNT@Co$_3$O$_4$, CNT/Co$_3$O$_4$ nanocomposite, and pristine CNT air electrodes at different current densities at the same cut-off capacity of 300 mAh g^{-1}.

ADVANCED
SCIENCE NEWS
www.advancedsciencenews.com

ADVANCED
FUNCTIONAL
MATERIALS
www.afm-journal.de

air electrodes, respectively, indicating improved kinetics in the initial stage of the ORR as a result of Co_3O_4.

On the other hand, when comparing the OER processes of the three air electrodes, it can be observed that introducing active catalyst centers significantly increases the decomposition rate of the discharge products during charging, and increases the round-trip efficiency of $CNT@Co_3O_4$ and CNT/Co_3O_4 air electrodes. All three charging curves can be divided into three regions: (1) a plateau around 2.6 V, (2) a short slope between 3.7 and 4.0 V, and (3) another slope or plateau above 4.0 V. Region (1) is generally assigned to the decomposition of NaO_2,[21–24,27] while regions (2) and (3) are believed to be associated with the decomposition of Na_2O_2[16,17,22] and/or Na_2CO_3.[16,56] For region (3), at around 0.3 and 0.4 V, overpotential reductions were found in the charging curves of $CNT@Co_3O_4$ and CNT/Co_3O_4 air electrodes, respectively, which are consistent with the corresponding value (400 mV) that was observed for a Co_3O_4-based catalyst in $Li–O_2$ batteries,[29,30,43] implying a similar OER catalyst activity of Co_3O_4 toward both sodium and lithium peroxides. Besides, the 0.6 V polarization of region (1) of the charging process of pristine CNT air electrode reduces to around 0.4 V in the cases of both CNT/Co_3O_4 and $CNT@Co_3O_4$ air electrodes. These results indicate that the Co_3O_4 catalyst can contribute to the OER of decomposing not only the peroxide in discharge product, as widely observed in a $Li–O_2$ battery, but also the superoxide NaO_2 phases as discharge product produced in the $Na–O_2$ batteries. A more detailed analysis of these findings will be presented in the subsequent part of this study. It should be noted that although it is generally found that the intrinsic overpotential to electrochemically decompose sodium superoxide NaO_2 can be very low, rapid increased charging overpotentials are still observed when the high current densities have been applied,[24,57] especially in the absence of proton sources in the electrolyte.[58] Accordingly, our achieved results imply that catalyst(s) may still be essential in order to further promote the performance of SABs for high current rate applications.

The electrochemical performance of $CNT@Co_3O_4$ and CNT/Co_3O_4 air electrodes were also examined using different current densities; typical voltage profiles are shown in Figure 3c,d. The $CNT@Co_3O_4$ air electrode exhibited a first discharge (charge) capacity of 715 (600), 624 (619), and 313 (299) mAh g^{-1} at 150, 300, and 500 mA g^{-1}, respectively. In comparison, the corresponding discharge (charge) capacity of CNT/Co_3O_4 air electrodes at same current density were found to be 557 (488), 489 (420), and 291 (246) mA g^{-1}, respectively. Apparently, $CNT@Co_3O_4$ air electrodes show improved discharge capacity and Coulombic efficiency when compared to CNT/Co_3O_4 air electrodes, indicating that ALD Co_3O_4 has enhanced OER and ORR catalytic performance as well as reduced amount of residential undecomposed discharge product following charging. Besides, a short spike at the initial stage of the discharge can be observed in all of the cycling profiles of the CNT/Co_3O_4 air electrode (Figure 3d), which, in contrast, was not observed in the corresponding curves of $CNT@Co_3O_4$ (Figure 3c). This should be attributed to the improved electrical contact between well-dispersed ALD Co_3O_4 and the underlying CNT substrate, as discussed above and supported by the SEM images. Interestingly, the charge curves of the $CNT@Co_3O_4$ air electrodes at 150 and 300 mA g^{-1} nearly overlapped, in spite of the larger discharge capacity at the lower

current density. This phenomenon suggests an inadequate removal of the discharge product in the air electrode. Hartmann et al. suggested that the OERs in SABs, i.e., the electrochemical removal of discharge product, preferred to occur at the adherent surface between sodium superoxide and carbon cathode substrate and this process results in the cutoff of electron transfer after a certain stage of charging and leads to the incomplete decompose of sodium superoxide after charging.[24,25]

The cycling performance of $CNT@Co_3O_4$ air electrode was also tested by its charge and discharge measurements using a cut-off capacity of 300 mAh g^{-1} at different current densities. An increasing trend was found in the charge capacity of the voltage plateau occurring at around 2.5 V, which is consistent with our previous report.[21,29] At a low current density of 75 mA g^{-1}, the voltage plateau at 2.5 V is barely visible, implying a very low proportion of superoxide species in the corresponding discharged electrode, possibly due to disproportionation reactions occurring. At a high current density of 500 mA g^{-1}, the charge capacity of the cell was below 300 mAh g^{-1}, indicating incomplete removal of the discharge product. Thus, it is anticipated that the optimized electrochemical performance of $CNT@Co_3O_4$ air electrode could be achieved at a medium current density at the same depth of discharge. As expected, $CNT@Co_3O_4$ air electrode exhibited longer cycling lives when compared to pristine CNT and CNT/Co_3O_4 air electrodes (Figure 3f). From the charge and discharge curves of all three air electrodes at a current density of 150 mA g^{-1} and a cut-off capacity of 300 mAh g^{-1} (Figure S1, Supporting Information), it can be observed that the voltage curves of $CNT@Co_3O_4$ air electrode display increased stability compared to the other two electrodes, despite their similar cycling lives of 13–14 cycles. This fact suggests that additional features such as dendrite growth on Na anode[59] and/or electrolyte degradation of electrolyte[60–62] may have triggered the failure of the cells. Although ether-based electrolytes have been widely used in LABs and SABs, they have been also found to be not fully stable especially during long-term cyclings, which is believed to be a remaining challenge for LABs and SABs.[63–70] Bruce and co-workers found that Li_2CO_3, HCO_2Li, CH_3CO_2Li, polyethers/esters, CO_2, and H_2O are the decomposition products of the side reaction in LABs using linear-chain ether-based electrolytes.[71] Nazar and co-workers experimentally investigated the degradation product of the decomposition reactions of DEGDME-based electrolyte in $Na–O_2$ batteries and found them to be sodium formate, methoxy(oxo)acetic anhydride, and Na_2CO_3.[72] These side reactions have not only continuously consumed the electrolyte to limit the long-term cycling stability of the batteries but also formed insolating products which may have clog the air electrode and prevent the electrochemical ORR reactions. The gradient change of the charge and discharge curves of CNT air electrodes are similar to what has been observed for CNTs in $Li–O_2$ batteries published by Nasybulin et al.,[73] who found decreasing yields of Li_2O_2 during the cycling and attributed this phenomenon to the formation of an interfacial passive layer.

2.2.3. Cyclic Voltammetry Measurements

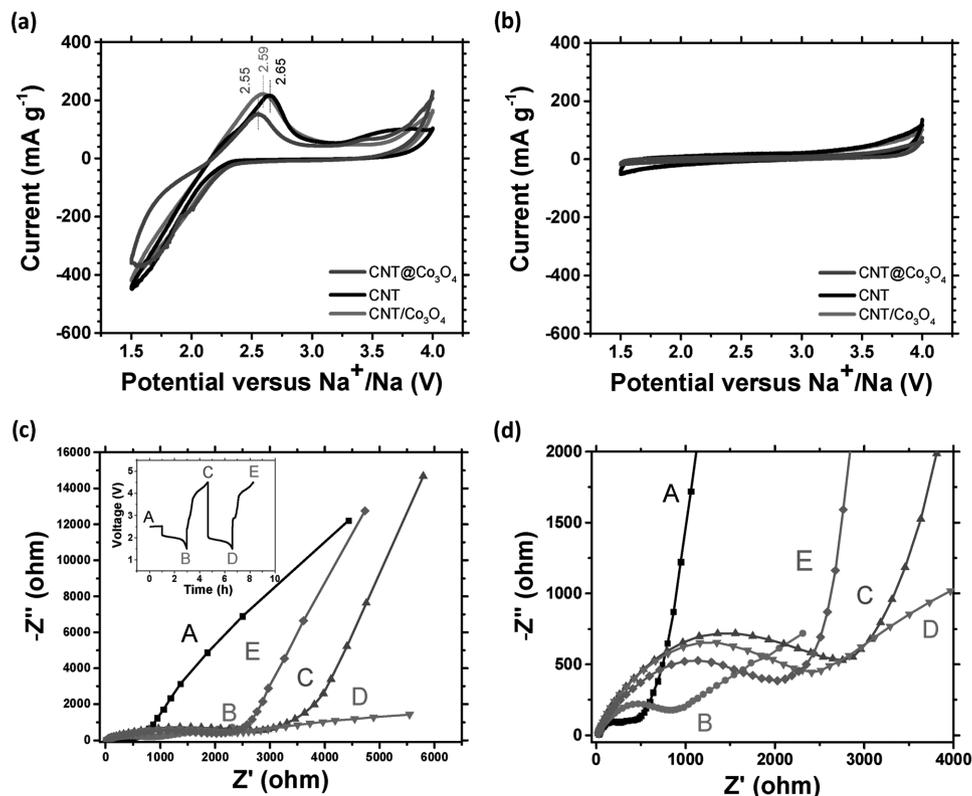The CV measurements also evidently demonstrate the improved ORR and OER capabilities brought by cobalt oxide

ADVANCED
FUNCTIONAL
MATERIALS
www.afm-journal.de

ADVANCED
SCIENCE NEWS
www.advancedsciencenews.com

FULL PAPER

Figure 4. CVs of ALD CNT@Co$_3$O$_4$, CNT/Co$_3$O$_4$ nanocomposite air electrodes, and pristine CNT under a) dried air and b) Ar. c,d) EIS spectra of SABs with ALD CNT@Co$_3$O$_4$ at initial, 1st, and 2nd discharged/charged states at a current density of 300 mA g^{-1}; inset of (c) shows the charge and discharge curves showing the state of charge/discharge for collecting EIS; (d) shows the low frequency region of (c).

catalyst (**Figure 4**a). The anodic current responses of all the three air electrodes were similar. However, the cathodic peaks of CNT@Co$_3$O$_4$ and CNT/Co$_3$O$_4$ air electrodes are shifted by 0.10 and 0.06 V lower than pristine CNT air electrodes. Besides, the CVs of all the three air electrodes under Ar did not show obvious current peaks (Figure 4b), which indicate that the redox currents can be predominantly attributed to reactions involving oxygen. Meanwhile, the Na ion intercalation into Co$_3$O$_4$ contributed negligible capacities in the corresponding voltage range. The CV results are consistent with charge and discharge behavior of the air electrodes and indicate the enhanced OER activities of CNT@Co$_3$O$_4$ and CNT/Co$_3$O$_4$ air electrodes.

2.2.4. Electrochemical Impedance Spectroscopy Measurements

EIS measurements were carried out on a SAB with CNT@Co$_3$O$_4$ air electrode at different charge and discharge stages. The Nyquist plots of initial, discharged, and charged cells are displayed in Figure 4c, which display depressed semicircles at high frequencies, related to the combination of resistor (charge-transfer resistance, R_{ct}) with a constant phase element standing for the surface double-layer capacitance, and a linear spike at low frequencies, which can be described as semifinite Warburg impedance associated to the diffusion of oxygen. It can be observed that the line slope in the low frequency section of the EIS spectra for the initial, 1st, and 2nd charged electrodes

are close to 45°, while the corresponding value of the discharged electrodes were also consistent and much lower than the former value, implying an alternate diffusion path. These results suggest that the termination of the oxygen reduction during discharge should be attributed to the blocking effect of oxygen by the coverage of the discharge products on the surface of the air electrode; and the reversible removal of the discharge product during charging enabled the subsequent cycling of the cell. In addition, a close observation of the low frequency portion of the EIS spectra (Figure 4d) further reveals the change of the R_{ct} for the air electrodes. The R_{ct} for the first discharged air electrode was only slightly larger than the initial one. However, the value of R_{ct} significantly increases after the first charge, and gradually decreases with subsequent cycling. The increased R_{ct} during the first charging process may be related to the formation of carbonates,[74] which might be a result of incomplete decomposition of sodium oxides and/or decomposition of electrolyte at elevated voltages.

2.3. Elucidating the Electrochemical Reaction Mechanism

2.3.1. Fourier-Transform Infrared Spectroscopy Characterization

In order to further reveal the composition of the discharge product(s) and the role of the catalyst in SABs, we systemically examined the IR absorptions of the original, discharged, and

**ADVANCED
SCIENCE NEWS**
www.advancedsciencenews.com

**ADVANCED
FUNCTIONAL
MATERIALS**
www.afm-journal.de

FULL PAPER

charged electrodes as well as reference Co_3O_4, Na_2O_2, Na_2CO_3, and $NaCF_3SO_3$ powders. The results are shown in **Figure 5**. The FT-IR spectra of Co_3O_4 demonstrates two strong absorption peaks at 567 and 665 cm^{-1} (Figure 5a), which correspond to the Co—O stretching vibration mode and O—Co—O bridging vibration mode,[75] respectively. Interestingly, the FT-IR spectra of CNT@Co_3O_4 showed only the strong absorption at 567 cm^{-1} (Figure 5f), implying a chemical interaction between the CNT substrate and ALD Co_3O_4. More surprisingly, the missing absorption at 665 cm^{-1} appeared in the IR spectra of the discharged CNT@Co_3O_4 electrode (Figure 5g). Meanwhile, the absorption of Co—O stretching vibration greatly weakened after discharge. After charging, the peak corresponding to Co—O stretching vibration recovered in the FT-IR spectra of the

CNT@Co_3O_4 electrode, along with a disappearance of the peak corresponding to O—Co—O bridging vibration (Figure 5h). In contrast, the discharged and charged CNT/Co_3O_4 electrodes did not show significant change in the same low wavenumber region (500–700 cm^{-1}) of their IR spectra (Figure 5i,j). This comparison indicates that the ALD-deposited Co_3O_4 is more actively involved in the electrochemical behavior of SABs, due to its chemical bond with the underlying CNT substrate. In other words, intermediate phase(s) has (have) formed during the ORR process. This is also consistent with the improved electrochemical performance of the CNT@Co_3O_4 compared to bare CNT or mechanical mixed CNT/Co_3O_4 air electrodes.

Additionally, when comparing the FT-IR spectra of the cycled air electrodes with the standard spectra of Na_2O_2 and Na_2CO_3 samples, apparent differences were observed. The IR absorptions centered around 1430 cm^{-1} could be found in all discharged CNT air electrodes (Figure 5g,i,k), corresponding to the formation of $Na_2O_2.2H_2O$,[19] which can be attributed to the chemical reaction between water impurities and discharge product Na_2O_2[21] or NaO_2.[57] Besides, the IR absorption at 882 cm^{-1} related to ν_2 mode of Na_2CO_3[76] was also observed in the discharged CNT air electrode (Figure 5k). However, the relative intensity of this peak for CNT air electrode compared to other IR peaks was much stronger than those found for of CNT@Co_3O_4 and CNT/Co_3O_4 air electrodes. After charging, the corresponding absorption centered at 1430 cm^{-1} nearly vanishes in the IR spectra for CNT@Co_3O_4 and CNT/Co_3O_4 air electrodes. In contrast, although significantly weakened, an absorption peak can still be observed for charged CNT air electrode with a shift to 1455 cm^{-1}, which is completely consistent with the spectra of standard Na_2CO_3 (ν_3 mode of Na_2CO_3[76]). It can be concluded that an increased amount of Na_2CO_3 was formed during charging in the case of bare CNT air electrode, which is consistent with the study by McCloskey et al.[74] Overall, the evidence gathered from FT-IR measurements clearly demonstrate that introducing Co_3O_4 catalyst can effectively improve the OER ability of the CNT air electrode as well as suppressing the formation of and removal of the side products.
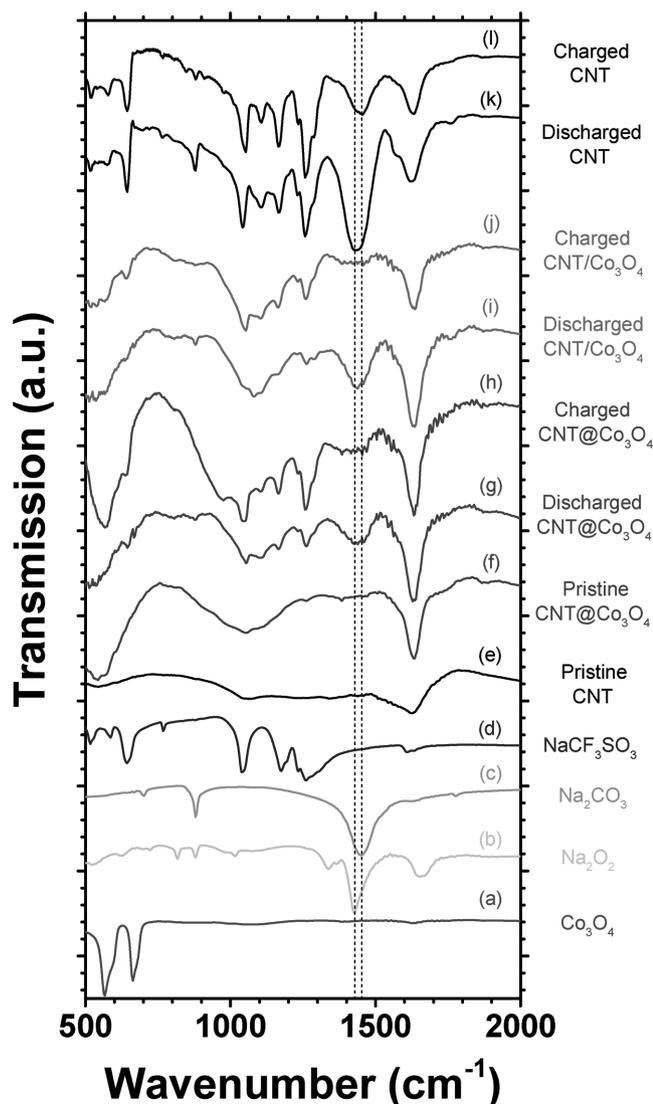
2.3.2. Morphological Characterization

SEM images of CNT@Co_3O_4 and CNT/Co_3O_4 air electrodes after being discharged at 150 and 300 mA g^{-1} are compared in **Figure 6**. A clear dissimilarity between the morphologies of the discharge products between each air electrode is visible. Well-uniform epitaxial growth of discharge product on the surface of CNT@Co_3O_4 can be found under both current densities of 150 and 300 mA g^{-1}. The EDX element mapping also provides clear evidence of the even distribution of Na-containing discharge product along the outer CNT@Co_3O_4 (**Figure 7I**). This core–shell structure is similar to our previous report on a nitrogen-doped CNT (NCNT) air electrode for SAB at low current rates.[23] This phenomenon may be possibly explained by the similarity between NCNT and CNT@Co_3O_4, where the simplified structure of NCNT, which can be considered as the CNT with surface active catalytic center (N-doping sites), is topologically equivalent to the CNT@Co_3O_4. However, the morphology of the discharge products formed on NCNT air electrodes did not maintain the

Figure 5. FT-IR spectra of standard a) Co_3O_4, b) Na_2O_2, c) Na_2CO_3, d) $NaCF_3SO_3$ (electrolyte salt), e) pristine CNT samples; f) as-deposited, g) first discharged and (h) first charged ALD CNT@Co_3O_4 air electrode; i) first discharged and j) first charged ALD CNT/Co_3O_4 nanocomposite electrode; k) first discharged and l) first charged pristine CNT air electrode. Dashed lines indicate the absorption position corresponding to Na_2O_2 and Na_2CO_3, respectively.

ADVANCED
FUNCTIONAL
MATERIALS
www.afm-journal.de

ADVANCED
SCIENCE NEWS
www.advancedsciencenews.com

FULL PAPER

CNT@Co$_3$O$_4$

150 mA/g

300 mA/g

CNT/Co$_3$O$_4$

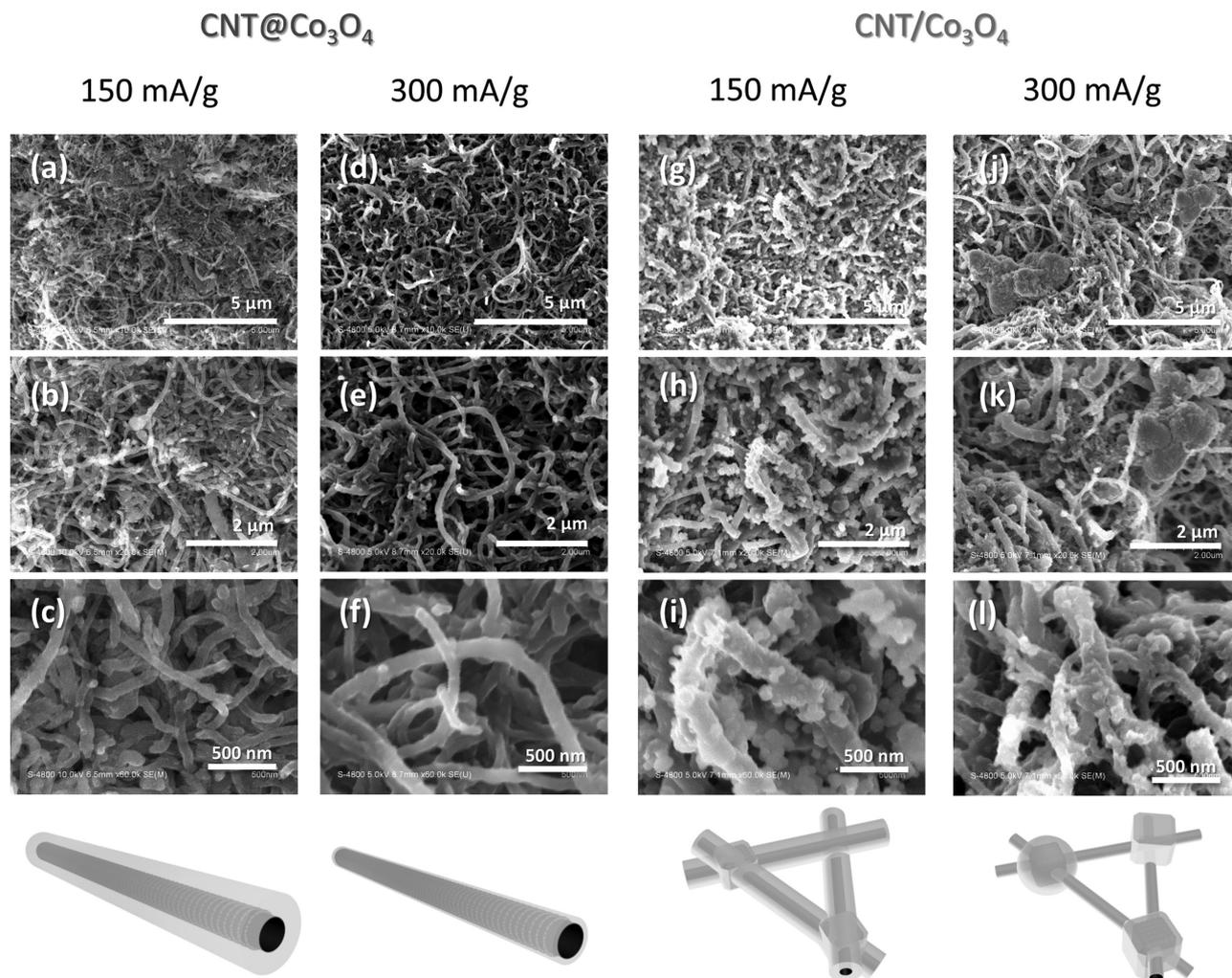150 mA/g

300 mA/g

Figure 6. Morphology of discharged a–f) ALD CNT@Co$_3$O$_4$ and g–l) CNT/Co$_3$O$_4$ nanocomposite air electrodes at the current densities of 150 and 300 mA g^{-1}. Schematic graphs are also shown.

similar core–shell structure under high current rates,[23] but rather formed nanorod-like structures similar to discharge product found for CNT/Co$_3$O$_4$ air electrodes presented here. This comparison infers further improvement for catalyst performance of CNT@Co$_3$O$_4$. On the other hand, irregular nanoparticles and nanorods were found for discharged CNT/Co$_3$O$_4$ air electrodes at a current density of 150 mA g^{-1}, while micron-sized box-like discharge products were observed in close proximity to nanoparticles formed on the single CNTs under 300 mA g^{-1}. Further EDX mapping analysis reveals the conformal growth of discharge products on CNTs at a low current rate for the CNT/Co$_3$O$_4$ air electrode (Figure 7II). However, under elevated current rates, despite of the coverage of discharge products over both CNTs and Co$_3$O$_4$ nanoclusters, the micron-sized boxes were found in both of the presence and absence of Co$_3$O$_4$ centers (Figure 7III), while the discharge products with this special shape are generally believed to be the NaO$_2$ phase.[24] Furthermore, after recharging, the morphology of both of the CNT@Co$_3$O$_4$ and CNT/Co$_3$O$_4$ air electrodes recovered (Figures S2 and S3, Supporting Information). It can be concluded that the solid-state product aggregated on the surface of CNT@Co$_3$O$_4$ air electrode in a more efficient

way than the CNT/Co$_3$O$_4$ one, which can reduce the blockage of oxygen gas releasing or ion diffusion during the cycling. This factor contributed to both of the increased capacity and round-trip efficiencies of former air electrode.

2.3.3. X-Ray Absorption Fine Structure Analysis

In order to further reveal the electronic and structural information of CNT@Co$_3$O$_4$ and CNT/Co$_3$O$_4$ air electrodes and their evolution during electrochemical processes, synchrotron-based XAS measurements were carried out to obtain Co K-edge X-ray absorption fine structure (XAFS). The normalized Co K-edge XAFS spectra of initial, discharged, and charged CNT@Co$_3$O$_4$ and CNT/Co$_3$O$_4$ air electrodes are shown in **Figure 8**a. It can be observed that the Co XAS of all electrodes exhibited a similar features and are well matched with Co K-edge XAS spectra reported in previous studies,[77–79] indicating that the Co species in the initial and electrochemical reacted air electrodes mainly exist as Co$_3$O$_4$. The X-ray absorption near edge structure (XANES) spectra of the air
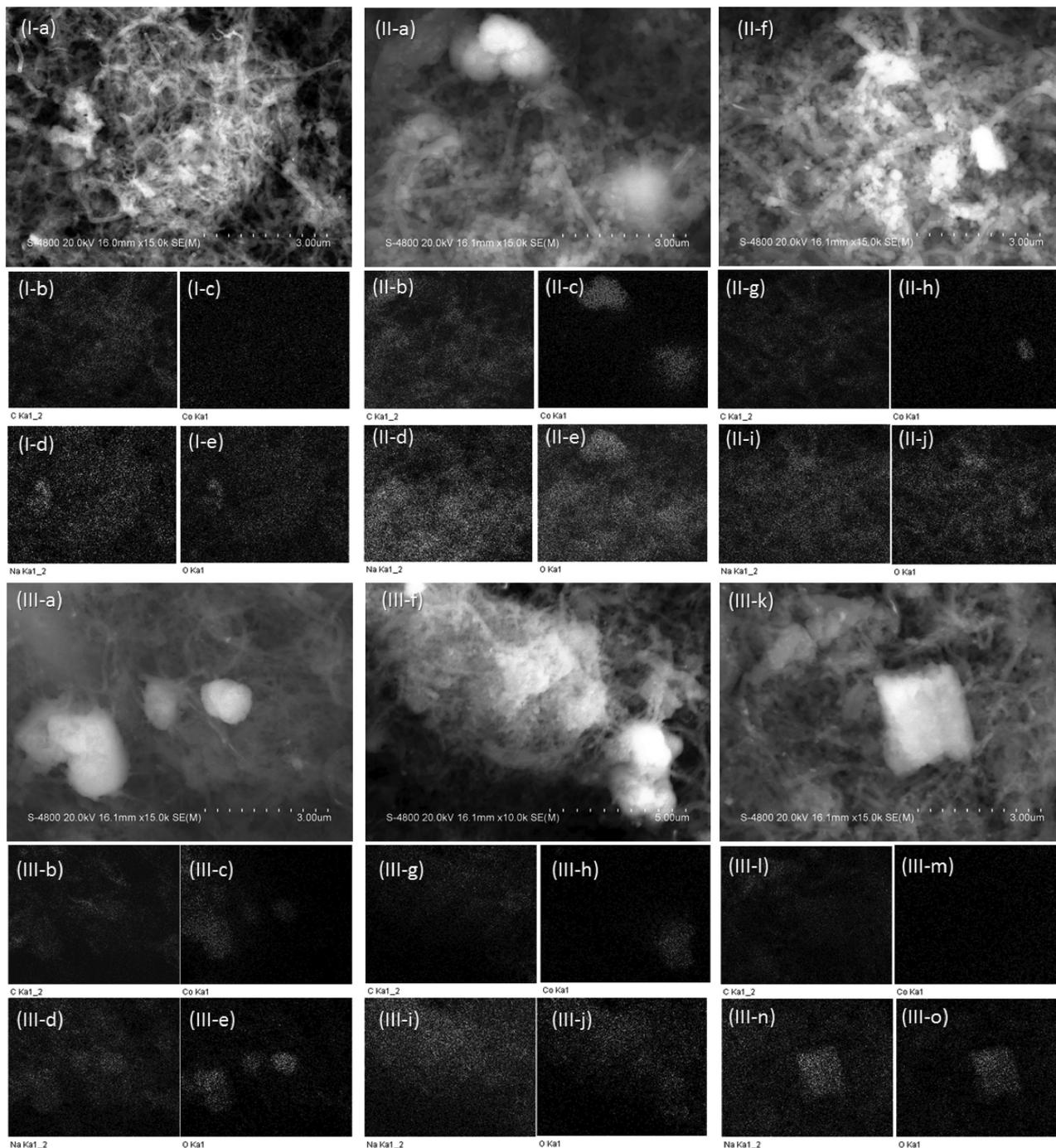
ADVANCED
SCIENCE NEWS
www.advancedsciencenews.com

ADVANCED
FUNCTIONAL
MATERIALS
www.afm-journal.de

FULL PAPER

Figure 7. I) a) SEM image of discharged ALD CNT@Co_3O_4 at 150 mA g^{-1}; EDX mapping in the corresponding region of b) C, c) Co, d) Na, and e) O elements. II) a,f) SEM image of two different regions of discharged CNT/Co_3O_4 nanocomposite at 150 mA g^{-1}; EDX mapping in the corresponding regions of b,g) C, c,h) Co, d,i) Na, and e,j) O elements. III) a,f,k) SEM image of three different regions of discharged CNT/Co_3O_4 nanocomposite at 300 mA g^{-1}; EDX mapping in the corresponding regions of b,g,l) C, c,h,m) Co, d,i,n) Na, and e,j,o) O elements.

electrodes (shown in Figure S4 in the Supporting Information) also clearly demonstrate that the oxidation state of these electrodes remain throughout the electrochemical process. These result are consistent with soft X-ray XAS studies of the Co L-edge on the application of Co_3O_4 as air electrode for Li–air batteries conducted by Yao et al.[80] They reported that

no obvious changes were observed for pristine, partial, and full charged Co_3O_4 catalyst.

However, following Fourier transformation of the extended X-ray absorption fine structure (EXAFS) in to R-space, noticeable distinctions can be observed between spectra obtained for CNT@Co_3O_4 and CNT/Co_3O_4 air electrodes. The distinction
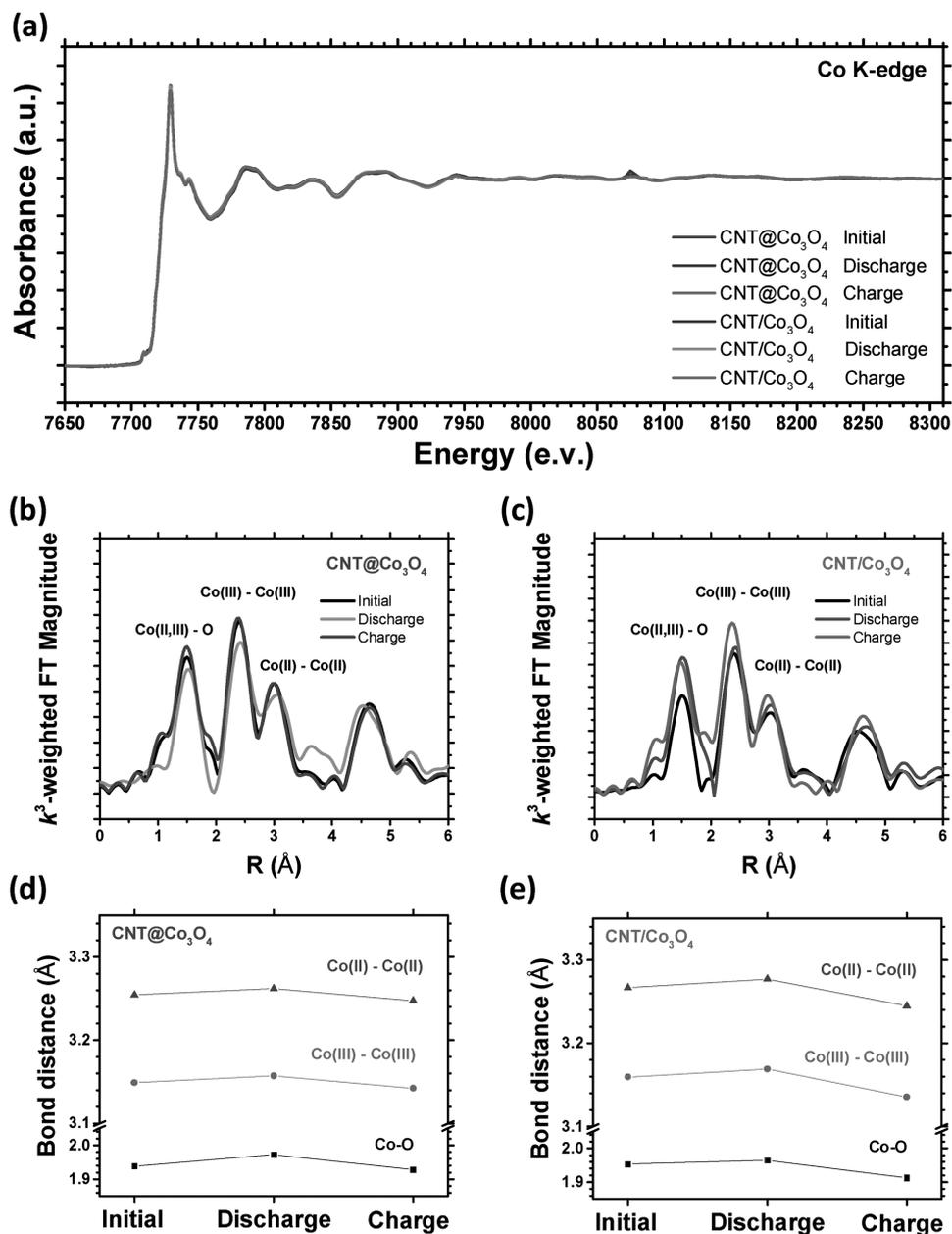
ADVANCED
FUNCTIONAL
MATERIALS
www.afm-journal.de

ADVANCED
SCIENCE NEWS
www.advancedsciencenews.com

Figure 8. a) Normalized Co K-edge XAS spectra of ALD CNT@Co$_3$O$_4$ and CNT/Co$_3$O$_4$ nanocomposite air electrodes at initial, first discharge, and first charge stages. Corresponding k^3-weighted Fourier transforms of the EXAFS spectra at the Co K-edge for initial, discharged, and charged b) ALD CNT@Co$_3$O$_4$ and c) CNT/Co$_3$O$_4$ nanocomposite air electrodes. Calculated bond distance between first shell Co—O, second shell Co(III)—Co(III), third shell Co(II)—Co(II) after fitting of d) ALD CNT@Co$_3$O$_4$ and e) CNT/Co$_3$O$_4$ nanocomposite air electrodes.

between the evolution of neighbor structures of Co ions in CNT@Co$_3$O$_4$ and CNT/Co$_3$O$_4$ air electrodes during the electrochemical processes that were further revealed by their Fourier transformed (FT) Co K-edge EXAFS spectra are shown in Figure 8b,c, respectively. The first shell of the R-space for Co EXAFS in Co$_3$O$_4$ is attributed to the Co—O coordination, while the 2nd and 3rd shells are attributed to Co(III)—Co(III) coordination in octahedral (Oh) symmetry and Co(II)—Co(II) coordination in tetrahedral (Td) symmetry, respectively.[77,78,81–83] For CNT@Co$_3$O$_4$ air electrodes, an alternate coordination feature is clearly observed upon discharge compared to the pristine

electrode from the shapes of the FT curves, which, nonetheless, nearly fully recovered after charging. However, for CNT/Co$_3$O$_4$ air electrode, the distance between Co center and 1st, 2nd, and 3rd coordinating shell irreversibly changes after discharge and charge processes. After fitting the experimental data, the bond distances of Co—O, Co(II)—Co(II), and Co(III)—Co(III) of CNT@Co$_3$O$_4$ and CNT/Co$_3$O$_4$ air electrodes before and after electrochemical processes were obtained and shown in Figure 8d,e, respectively. It can be observed that bonding between elements is slightly stretched following discharge, indicating a reduction of cobalt and/or oxygen in Co$_3$O$_4$. For

**ADVANCED
SCIENCE NEWS**
www.advancedsciencenews.com

*ADVANCED
FUNCTIONAL
MATERIALS*
www.afm-journal.de

FULL PAPER

ALD CNT@Co$_3$O$_4$ air electrode, these bonding distances well restored after charging as shown in Figure 8d, which is in good accordance with the FT curves. In contrast, the three bonding distances of the charged CNT/Co$_3$O$_4$ air electrode shift to a lower value than those found for the initial electrode, indicating an overcharged state of Co$_3$O$_4$. This difference between the two air electrodes should be attributed to the different adherent state between the Co$_3$O$_4$ catalyst center and CNT as conductive substrate. The core–shell structured ALD CNT@Co$_3$O$_4$ enables the rapid charge transferring between CNT and Co$_3$O$_4$ benefited from their Ohmic contact, while the stacked Co$_3$O$_4$ particles on CNTs in the CNT/Co$_3$O$_4$ air electrodes may have suffered from Schottky barrier between the semiconductive cobalt oxide and CNTs. Overall, these results suggest that the ALD Co$_3$O$_4$ may have benefited from stabilization and anchoring effect of CNT core. In contrast, the mechanically grinded Co$_3$O$_4$ may have suffered from negative effects such as irreversible dissolution of Co, Na ion incorporation into the lattice, and/or oxidation effect from discharge product superoxide. These XAS evidences provide more insight toward deeper understanding of the catalytic behavior of the Co$_3$O$_4$ catalysts for SABs.

2.3.4. STXM

The distribution of sodium peroxide/superoxide in discharged CNT@Co$_3$O$_4$ and CNT/Co$_3$O$_4$ air electrodes is revealed with the use of STXM. STXM combines microscopy technology with synchrotron-based XANES method, enabling nanoscale chemical imaging with a spatial resolution of around 30 nm as well as fine energy resolution. The detailed principle of STXM and the descriptions of the STXM configurations of the Spectromicroscopy (SM) beamline of the Canadian Light Source have been reported in previous studies.[84–88] The discharged electrodes were taken out from the dissembled cells and washed with DEGDME. The CNT/Co$_3$O$_4$/NaO$_x$ mixtures were then scraped off the substrates and dispersed in pure DEGDME solvent before drop-casted on to a transmission electron microscopy (TEM) grid inside an Ar-filled glovebox. Two chosen regions of discharged CNT@Co$_3$O$_4$ and CNT/Co$_3$O$_4$ samples were characterized by STXM at the O K-edge and Co L-edge, respectively. From the O K-edge XANES of different region of the two samples (Figures S5a and S6a, Supporting Information) and comparing with the corresponding spectra of standard materials (Figures S5b and S6b, Supporting Information),[87,89] the Co$_3$O$_4$, Na$_2$O$_2$, and NaO$_2$ phases can be clearly identified by their distinct features. The appearance of π^* orbital located at several eVs below σ^* orbital in the O K-edge XAS spectra indicates the existence of superoxide O$_2^-$, as we have shown in our previous study.[87,89] Meanwhile, the Co L-edge XANES provides the evidence of its elemental distributing information (Figures S5d and S6d, Supporting Information). For CNT@Co$_3$O$_4$ air electrode, the discharge product is found to be a uniform mixture of sodium peroxide and superoxide (denoted as NaO$_x$ (I)). In contrast, some regions in the discharged CNT@Co$_3$O$_4$ air electrode (e.g., region (4) in Figure S6a, Supporting Information) clearly exhibit a π^* orbital weakened feature (denoted as NaO$_x$ (II)) when compared to other regions (denoted as NaO$_x$ (III)), which should be related to alternate proportions of superoxide

NaO$_2$ to peroxide Na$_2$O$_2$. From the XAS patterns, it can be indicated that NaO$_x$ (I), (II), and (III) are composed of both NaO$_2$ to peroxide Na$_2$O$_2$ components. However, the different ratios of the intensities of the XAS peak corresponding to π^* and σ^* orbital in NaO$_x$ (I), (II), and (III) samples demonstrate their different superoxide and peroxide proportions. Therefore, it is possible to distinguish NaO$_2$-rich and Na$_2$O$_2$-rich regions in the discharged CNT@Co$_3$O$_4$ and CNT/ Co$_3$O$_4$ air electrode by identifying the mapping of different NaO$_x$ distributions in their STXM images, which can be further compared to the location of the Co$_3$O$_4$ catalysts.

Based on these XANES spectra, chemical mapping of O at K-edge and Co at L-edge of the two samples are collected by STXM and shown in **Figure 9**. The color scales of the figures represent the thickness distribution of the corresponding species. In the case of ALD deposited catalyst, it can be observed that the NaO$_x$ discharge product (I) uniformly covers the surface of CNT@Co$_3$O$_4$ (Figure 9c). A comparison of the distribution of Co and O in the mapping provides evidence for the consistency of STXM results (Figure 9c,f). In contrast, in the case of mechanically grinded sample, the NaO$_x$ (II) is found to mainly exist as large particle aggregates in the discharged CNT/Co$_3$O$_4$ air electrode, regardless of the existence of Co$_3$O$_4$ core. NaO$_x$ (III), on the other hand, is found likely to grow along the CNTs. These evidences clearly show that the distribution of catalyst plays an important role on the uniformity of discharge product. Meanwhile, the content of discharge product depositing on the surface of CNTs (likely to be a result of electrochemical growth) differs from those forming as individual particles (possibly as a result of participation from solution). To summarize, STXM mapping results are consistent with the above-discussed SEM EDX results and clarify the composition and distribution of the discharge products in the nanoscale.

2.4. Role of Catalysts in Na–Air Batteries

Based on all the above experimental evidence and analysis, we can begin to elucidate the role of catalysts in SAB. In comparison with Li–air batteries, the unique superoxide electrochemistry/chemistry in Na–air batteries indubitably perplexes its reaction mechanisms involving catalysts. Apparently, the electrochemical measurements have demonstrated improved OER/ORR capabilities and cycling stability after introducing Co$_3$O$_4$ as the catalyst. Our observations indicate that even though the overpotential to decompose superoxide phase NaO$_2$ electrochemically is already low, it can be further reduced after using Co$_3$O$_4$ catalyst. Meanwhile, the very close overpotentials of around 0.4 V were observed for both CNT@Co$_3$O$_4$ and CNT/ Co$_3$O$_4$ air electrodes, in spite of the fact that the cubic NaO$_2$ is not essentially located at a nearby position beside Co$_3$O$_4$. Nazar and co-workers have recently proven that proton play a critical role in the low overpotential used to decompose NaO$_2$, following the reaction routes of (1) NaO$_2$ + H$^+$ → HO$_2$ + Na$^+$ and (2) HO$_2$ – e → O$_2$ + H$^+$.[58] Siegel and co-workers suggested that dissolved Co^{2+} ions in electrolyte from solid-state Co$_3$O$_4$ phase may incorporate into the discharge product Li$_2$O$_2$ in a Li–oxygen battery to reduce the charging overpentential.[90] Ortiz-Vitoriano et al. predicted a much higher fraction of soluble NaO$_2$
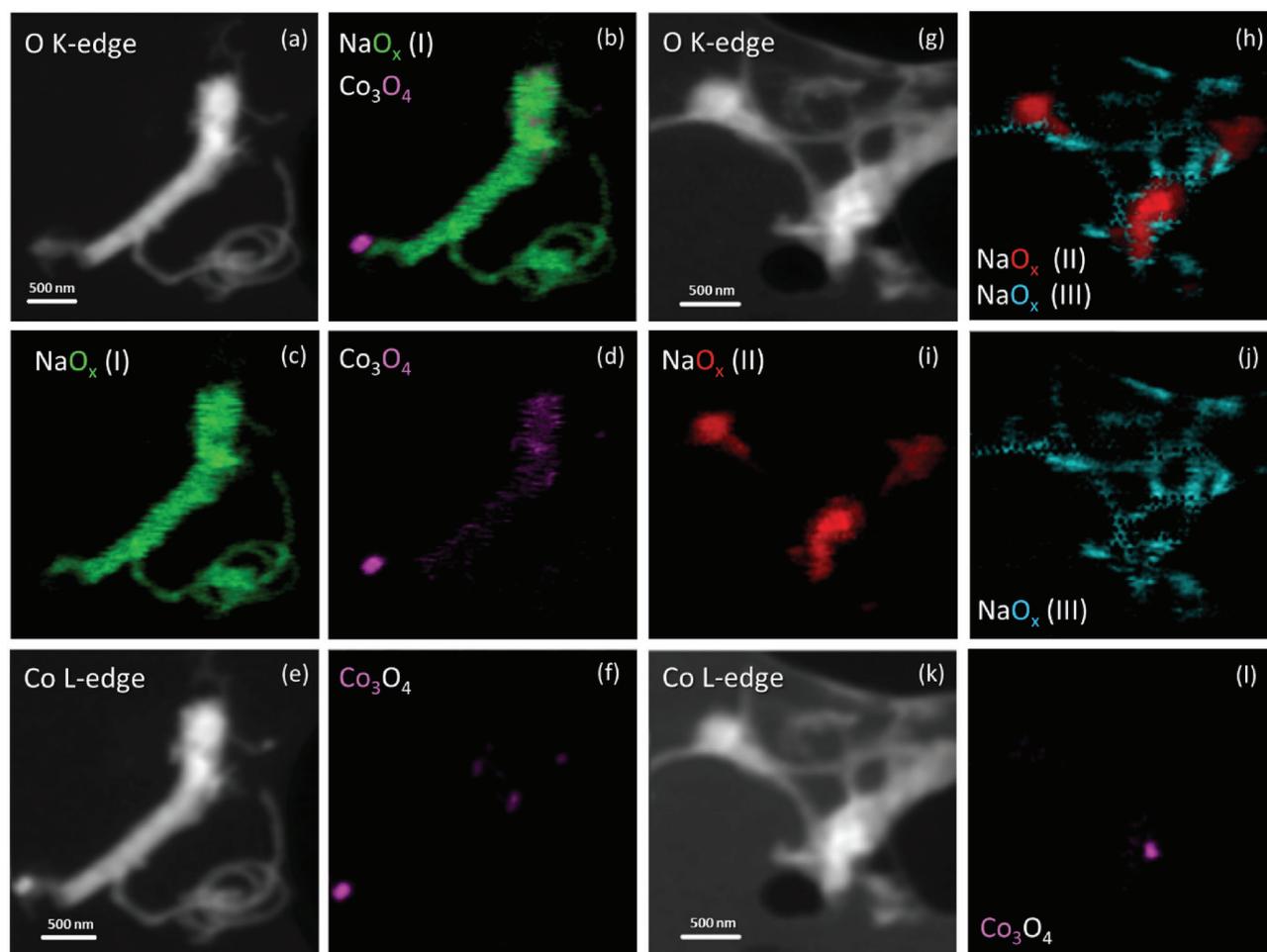
ADVANCED
FUNCTIONAL
MATERIALS
www.afm-journal.de

ADVANCED
SCIENCE NEWS
www.advancedsciencenews.com

FULL PAPER

Figure 9. a,g) O K-edge and e,k) Co L-edge optical density images (average stacks) of discharged ALD CNT@Co$_3$O$_4$ and g–l) CNT/Co$_3$O$_4$ nano-composite air electrodes. STXM chemical imaging of discharged b–d, f) ALD CNT@Co$_3$O$_4$ and h–j, l) CNT/Co$_3$O$_4$ nanocomposite air electrodes by extracting XANES spectra of Co$_3$O$_4$ and different types of NaO$_2$.

species in DME solvent than that of the LiO$_2$ based on the estimated calculation from the donor number (hard soft acid base theory) of the solvent.[57] Hartmann et al. also proposed that the micron-sized NaO$_2$ should be grown from the solution precipitation process as opposed to electrochemical pathway(s) based on experimental results.[91] Kang and co-workers calculated the tendency of NaO$_2$ dissolving in various electrolytes with different dielectric constants,[92] and revealed the practical dissolution and ionization process of sodium superoxide in the ether electrolyte.[93] Inspired by the above references and combining all the presented experiment results in this study, a similar redox reaction mechanism involving the dissolved cobalt ion in electrolyte can be proposed here. Co^{2+}/Co^{3+} ion pairs may react with dissolved HO$_2$ or Na$^+$O$_2^-$ species, acting as a redox mediator (RM) and may contribute to the improved OER kinetics. Soluble RM catalysts have been widely reported for Li–oxygen batteries.[94–97] Meanwhile, the build-up of micro-n-sized box-shape NaO$_2$ has also been proposed to be a result of crystal growth from dissolved Na$^+$ and O$_2^-$ in the previous study.[57] This is also supported by the fact that box-shaped products were mainly found for CNT/Co$_3$O$_4$ air electrode

discharged in the large current in this study. The large current densities cause supersaturation of dissolved superoxide species, leading to a random distribution of discharge product. In contrast, under low current densities, due to the lower adsorption energy of surface Co$_3$O$_4$ compared to carbon materials,[38] the dissolved superoxide species tend to be captured by the Co$_3$O$_4$ centers, where surface diffusion of superoxides can be further promoted.[43] Apparently, the even distribution of cobalt oxide in Co$_3$O$_4$@CNT resulted in a layer by layer aggregation of the discharge product. During charging, both dissolved Co^{2+}/Co^{3+} ions at the surface of Co$_3$O$_4$[40,98] can be expected to catalyze the decomposing of peroxide/superoxide. This assumption is also consistent with the removal of large micron-sized discharge product in CNT/Co$_3$O$_4$ air electrode. The systemic mechanisms of the OER/ORR processes and growth of discharge products are illustrated in **Figure 10**.

Another important factor to consider is the formation of carbonates during the first charging of SABs.[74,89] Black et al. reported that a dramatic increase of Li$_2$CO$_3$ was found in the initial stage of charging for Co$_3$O$_4$/RGO air electrode after discharging a Li–oxygen cell, which was subsequently removed

**ADVANCED
SCIENCE NEWS**
www.advancedsciencenews.com

**ADVANCED
FUNCTIONAL
MATERIALS**
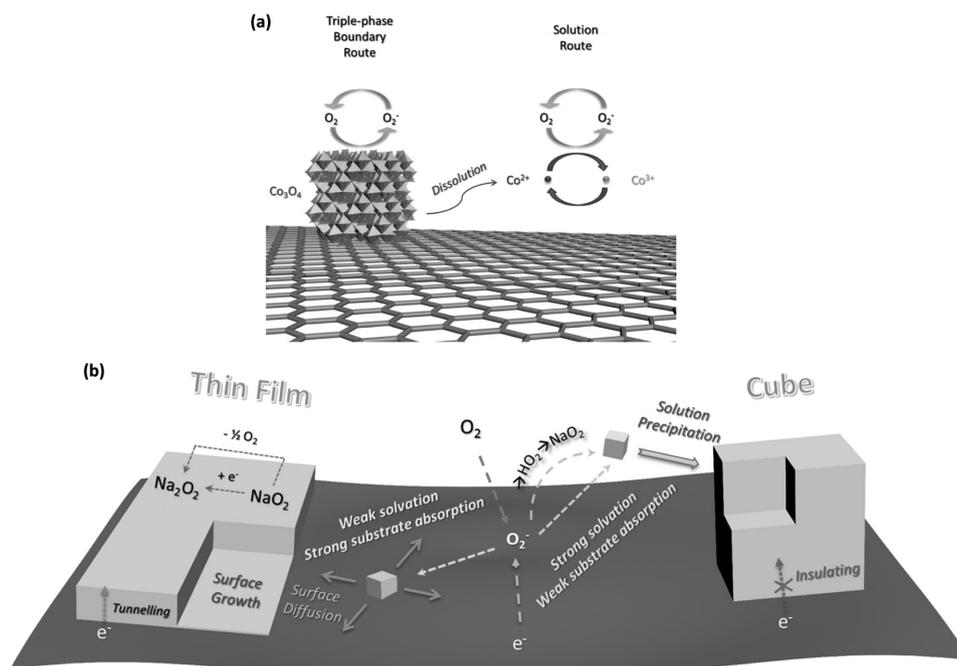www.afm-journal.de

FULL PAPER

Figure 10. Schematic diagrams of the a) catalyst mechanism of CNT@Co$_3$O$_4$ and b) growth mechanism of discharge products. Atomic layer deposition (ALD) is applied for artificial rational design of catalyst for Na–air batteries. ALD CNT@Co$_3$O$_4$ substrate shows significant improved OER and ORR activities and extended cycling lives than pristine CNT air and mechanically grinded CNT/Co$_3$O$_4$ electrodes. The role of the catalyst in Na–air batteries is revealed and clarified.

during the following charging process.[43] Here, it is evidenced by the IR results in this study, demonstrating that the removal of these carbonates in the presence of Co$_3$O$_4$ was more efficient. It has been also reported that Au[99] or NiO[100] catalysts can promote the decomposing of Li$_2$CO$_3$ in Li–O$_2$ batteries to increase the cycling stabilities of the cells. Analogously, it should be alleged that the consideration of carbonate elimination will be also critical in the future design of catalyst for SABs.

Overall, the present study demonstrates the fabrication of uniformly dispersed Co$_3$O$_4$ on CNTs by ALD and its superior electrochemical performance compared to pristine CNT and mechanically mixed CNT/Co$_3$O$_4$ air electrodes. The results suggest that introducing catalyst to air electrodes is an effective way to promote ORR and OER kinetics of SABs. The effect of catalyst is not only limited to solid-phase reactions but may also involve a liquid route in electrolyte, as well as play an important role in the morphologies of resulted discharge products. These results can contribute to the better understanding of catalysts for SABs. Finally, although 1D nanostructured CNTs are used as the supporting substrate for Co$_3$O$_4$ catalyst in this study, it is well known that ALD can be adopted for more sophisticated substrates. It can be expected that a 3D nanostructured air electrode will be built and applied in sodium–air battery in future work.

3. Conclusion

In this work, ALD has been successfully applied to fabricate CNT@Co$_3$O$_4$ as a non-noble metal oxide catalyst for SABs, while its electrochemical performance is compared to those of the mechanically grinded CNT/Co$_3$O$_4$ nanocomposite and

pristine CNT air electrodes. Both ALD and mechanically grinded Co$_3$O$_4$+CNT catalysts have contributed to reducing overpotentials toward OER and retained less discharge product following charging in SABs when compared to the pristine CNT air electrode. CNT@Co$_3$O$_4$ air electrodes exhibited increased capacity and extended cycling life due to the highly efficient utilization of well-dispersed catalytic centers as well as orientated growth of discharge product(s). The role of Co$_3$O$_4$ catalyst in SABs has been found to be able to promote the electrochemical decomposition of sodium peroxide, superoxide, and carbonates. This study demonstrates the potential of ALD as a powerful tool to construct hierarchical nanostructured catalyst for SABs. Moreover, various synchrotron-based characterization methods, including hard XAS and soft X-ray STXM, have been applied to analyze the reaction mechanism in the SABs. The hard XAS results indicate that the cobalt oxide in ALD CNT@Co$_3$O$_4$ catalyst exhibited better reversibility during cycling than that in mechanically grinded CNT/Co$_3$O$_4$ nanocomposite catalyst. Meanwhile, the soft X-ray STXM mapping, together with SEM and EDX mapping, reveal that the different solution-based and surface-based reaction mechanisms have been changed in the presence or absence of catalyst. These new understandings on the reaction mechanism and the role of catalyst in SABs are believed to be able to contribute to the future rational design of novel catalyst for these batteries.

4. Experimental Section

ALD: Commercial CNT powders were first refluxed with 70% nitric acid solution at 110 °C for 3 h to remove resident metal catalyst during its growth process and create surface functional groups to facilitate

ADVANCED
FUNCTIONAL
MATERIALS

www.afm-journal.de

ADVANCED
SCIENCE NEWS

www.advancedsciencenews.com

FULL PAPER

the initial ALD growth. Deposition of Co_3O_4 on CNTs by ALD was performed in a commercial ALD reactor (Savannah 100, Ultratech/ Cambridge Nanotech Inc., USA) by using cobaltocene ($CoCp_2$) and O_2 as precursors. $CoCp_2$ was heated to 95 °C in order to supply sufficient vapor for the deposition of Co_3O_4. The ALD manifold was kept at 150 °C to prevent precursor condensation, while O_2 was kept at room temperature. Nitrogen gas (99.999% in purity) was used as a carrier gas with a flow rate of 20 sccm, and the ALD reactor was maintained at a low level of base pressure (typically 0.38–0.49 Torr) by a vacuum pump (Pascal 2005 I, Adixen). The deposition temperature for ALD-Co_3O_4 was 350 °C. One ALD cycle was executed with the following six steps: (1) a supply of $CoCp_2$ with 0.5 s; (2) a 3.0 s extended exposure of $CoCp_2$; (3) a 15 s purge of remaining $CoCp_2$ and any byproducts; (4) a supply of O_2 with 1 s; (5) a 3.0 s extended exposure of O_2; (6) a 15 s purge of excess O_2 and any products. Co_3O_4 was deposited on CNTs by using 400 ALD cycles.

Fabrication of Air Electrode and Cells: The method of the fabrication of air electrodes was similar as the previous study report of Sun et al.[23] ALD CNT@Co_3O_4, mechanically grinded CNT/Co_3O_4 nanocomposite, and pristine CNT powders were mixed with polyvinylidene fluoride binder, sonicated in a *N*-methylpyrrolidinone solvent to disperse, and dipped and casted on a commercial PP porous separator film substrate. The films were then cut into round pieces with a diameter of 3/8 in. for assembling the cell. The gravimetric capacity of the air batteries was calculated based on the total weights of CNT and Co_3O_4 in the air electrode. The Co_3O_4 contents of ALD CNT@Co_3O_4, mechanically grinded CNT/Co_3O_4 were 15.39 and 10 wt%, respectively. The masses of the active materials in the air electrodes ranged between 0.25 ± 0.10 mg.

Electrochemical Measurements: The sodium–air batteries were tested with Swagelok-type cells as described in the previous paper.[11–14] A round metallic sodium foil with diameter of 3/8 in. was used as anode, covered by a PP separator (Celgard 3501) and an air electrode, as well as a stainless steel mesh current collector. 0.5 M sodium triflate ($NaSO_3CF_3$, Aldrich) was dissolved in DEGDME (Aldrich) and used as the electrolyte. The DEGDME solvents were dried over molecular sieves (4 Å, Aldrich) for at least one month before use. The discharge/charge characteristics were performed using an Arbin BT-2000 battery station in a sealed box filled with a 1.0 atm dried air atmosphere at room temperature (25 °C). Molecular sieves were placed in the testing container to achieve a dry air environment. Cyclic voltammetry and electrochemical impedance spectroscopy measurements were carried out with a multipotentiostat (VMP3, Biologic).

Physical Characterizations: Hitachi S-4800 field-emission scanning electron microscope was used to observe the morphologies of the pristine materials and air electrodes. XRD patterns were recorded using a Bruker D8 Advance (Cu-Kα source, 40 kV, 40 mA) spectrometer. FT-IR spectra were recorded using a Nicolet 380 (Thermo Scientific). To fabricate charge/discharged samples, the SAB cells were dissembled in an Ar-filled glovebox. The air electrode was washed with pure DEGDME and dried before measurements.

X-Ray Absorption Spectroscopy: XAFS measurements at the Co K-edge adsorption spectra were performed on the 06ID superconducting wiggler sourced hard X-ray microanalysis (HXMA) beamline at the Canadian Light Source with a premirror – double crystal monochromator – postmirror configuration using Si (111) crystals and Rh mirrors. Measurements were made at room temperature in fluorescence mode using a 32-element Ge detector. Metal Co foil was used for energy calibration.

Scanning Transmission X-Ray Microscopy: To prepare STXM samples, the active materials and discharge products in discharged air electrode were scraped off the substrates, dispersed in pure DEGDME, and then drop-casted on a TEM grid. STXM experiment was carried out at the Soft X-ray SM beamline of the Canadian Light Source (CLS). STXM data were analyzed by aXis2000 (available free for noncommercial applications at http://unicorn.mcmaster.ca/aXis2000.html). Chemical mappings were achieved by fitting the stacks with linear reference spectra of the standard XANES. The detailed descriptions of the CLS and SM beamline can be found in previous other reports.[86,87,101–104,88,105]

Supporting Information

Supporting Information is available from the Wiley Online Library or from the author.

Acknowledgements

[1] B. L. Ellis, L. F. Nazar, *Curr. Opin. Solid State Mater. Sci.* **2012**, *16*, 168.

[2] V. Palomares, P. Serras, I. Villaluenga, K. B. Hueso, J. Carretero-Gonzalez, T. Rojo, *Energy Environ. Sci.* **2012**, *5*, 5884.

[3] V. Palomares, M. Casas-Cabanas, E. Castillo-Martinez, M. H. Han, T. Rojo, *Energy Environ. Sci.* **2013**, *6*, 2312.

[4] M. D. Slater, D. Kim, E. Lee, C. S. Johnson, *Adv. Funct. Mater.* **2012**, *23*, 947.

[5] N. Yabuuchi, K. Kubota, M. Dahbi, S. Komaba, *Chem. Rev.* **2014**, *114*, 11636.

[6] H. Kim, J. Hong, K.-Y. Park, H. Kim, S.-W. Kim, K. Kang, *Chem. Rev.* **2014**, *114*, 11788.

[7] A. C. Luntz, B. D. McCloskey, *Chem. Rev.* **2014**, *114*, 11721.

[8] P. G. Bruce, S. A. Freunberger, L. J. Hardwick, J.-M. Tarascon, *Nat. Mater.* **2012**, *11*, 19.

[9] J. Wang, Y. Li, X. Sun, *Nano Energy* **2013**, *2*, 443.

[10] J. Lu, L. Li, J.-B. Park, Y.-K. Sun, F. Wu, K. Amine, *Chem. Rev.* **2014**, *114*, 5611.

[11] E. Peled, D. Golodnitsky, R. Hadar, H. Mazor, L. Goor, L. Burstein, *J. Power Sources* **2013**, *244*, 711.

[12] S. Ha, J.-K. Kim, A. Choi, Y. Kim, K. T. Lee, *ChemPhysChem* **2014**, *15*, 1971.

[13] S. K. Das, S. Lau, L. A. Archer, *J. Mater. Chem.* **2014**, *2*, 12623.

[14] P. Adelhelm, P. Hartmann, C. L. Bender, M. Busche, C. Eufinger, J. Janek, *Beilstein J. Nanotechnol.* **2015**, *6*, 1016.

[15] I. Landa-Medrano, C. Li, N. Ortiz-Vitoriano, I. R. de Larramendi, T. Rojo, J. Carrasco, *J. Phys. Chem. Lett.* **2016**, *7*, 1161.

[16] Q. Sun, Y. Yang, Z.-W. Fu, *Electrochem. Commun.* **2012**, *16*, 22.

**ADVANCED
SCIENCE NEWS**

www.advancedsciencenews.com

**ADVANCED
FUNCTIONAL
MATERIALS**

www.afm-journal.de

FULL PAPER

[17] W. Liu, Q. Sun, Y. Yang, J.-Y. Xie, Z.-W. Fu, *Chem. Commun.* **2013**, *49*, 1951.

[18] W.-M. Liu, W.-W. Yin, F. Ding, L. Sang, Z.-W. Fu, *Electrochem. Commun.* **2014**, *45*, 87.

[19] J. Kim, H.-D. Lim, H. Gwon, K. Kang, *Phys. Chem. Chem. Phys.* **2013**, *15*, 3623.

[20] Y. Li, H. Yadegari, X. Li, M. N. Banis, R. Li, X. Sun, *Chem. Commun.* **2013**, *49*, 11731.

[21] H. Yadegari, Y. Li, M. N. Banis, X. Li, B. Wang, Q. Sun, R. Li, T.-K. Sham, X. Cui, X. Sun, *Energy Environ. Sci.* **2014**, *7*, 3747.

[22] Y. Hu, X. Han, Q. Zhao, J. Du, F. Cheng, J. Chen, *J. Mater. Chem.* **2015**, *3*, 3320.

[23] Q. Sun, H. Yadegari, M. N. Banis, J. Liu, B. Xiao, B. Wang, S. Lawes, X. Li, R. Li, X. Sun, *Nano Energy* **2015**, *12*, 698.

[24] P. Hartmann, C. L. Bender, M. Vračar, A. K. Dürr, A. Garsuch, J. Janek, P. Adelhelm, *Nat. Mater.* **2013**, *12*, 228.

[25] P. Hartmann, C. L. Bender, J. Sann, A. K. Dürr, M. Jansen, J. Janek, P. Adelhelm, *Phys. Chem. Chem. Phys.* **2013**, *15*, 11661.

[26] P. Hartmann, D. Grübl, H. Sommer, J. Janek, W. G. Bessler, P. Adelhelm, *J. Phys. Chem. C* **2013**, *118*, 1461.

[27] C. L. Bender, P. Hartmann, M. Vračar, P. Adelhelm, J. Janek, *Adv. Energy Mater.* **2014**, *4*, 1301863.

[28] J. Lu, Y. J. Lee, X. Luo, K. C. Lau, M. Asadi, H.-H. Wang, S. Brombosz, J. Wen, D. Zhai, Z. Chen, J. D. Miller, Y. Sub Jeong, J.-B. Park, Z. Z. Fang, B. Kumar, A. Salehi-Khojin, Y.-K. Sun, A. L. Curtiss, K. Amine, *Nature* **2016**, *529*, 377.

[29] Y. Lei, J. Lu, X. Luo, T. Wu, P. Du, X. Zhang, Y. Ren, J. Wen, D. J. Miller, J. T. Miller, Y.-K. Sun, J. W. Elam, K. Amine, *Nano Lett.* **2013**, *13*, 4182.

[30] J. Lu, Y. Lei, K. C. Lau, X. Luo, P. Du, J. Wen, R. S. Assary, U. Das, D. J. Miller, J. W. Elam, H. M. Albishri, D. A. El-Hady, Y.-K. Sun, L. A. Curtiss, K. Amine, *Nat. Commun.* **2013**, *4*, 2383.

[31] X. Meng, X.-Q. Yang, X. Sun, *Adv. Mater.* **2012**, *24*, 3589.

[32] J. Liu, X. Sun, *Nanotechnology* **2015**, *26*, 024001.

[33] B. J. O'Neill, D. H. K. Jackson, J. Lee, C. Canlas, P. C. Stair, C. L. Marshall, J. W. Elam, T. F. Kuech, J. A. Dumesic, G. W. Huber, *ACS Catal.* **2015**, *5*, 1804.

[34] J. Xie, X. Yao, I. P. Madden, D.-E. Jiang, L.-Y. Chou, C.-K. Tsung, D. Wang, *J. Am. Chem. Soc.* **2014**, *136*, 8903.

[35] M. A. Schroeder, A. J. Pearse, A. C. Kozen, X. Chen, K. Gregorczyk, X. Han, A. Cao, L. Hu, S. B. Lee, G. W. Rubloff, M. Noked, *Chem. Mater.* **2015**, *27*, 5305.

[36] N. Cheng, M. N. Banis, J. Liu, A. Riese, X. Li, R. Li, S. Ye, S. Knights, X. Sun, *Adv. Mater.* **2015**, *27*, 277.

[37] N. Cheng, M. N. Banis, J. Liu, A. Riese, S. Mu, R. Li, T.-K. Sham, X. Sun, *Energy Environ. Sci.* **2015**, *8*, 1450.

[38] C. Shang, S. Dong, P. Hu, J. Guan, D. Xiao, X. Chen, L. Zhang, L. Gu, G. Cui, L. Chen, *Sci. Rep.* **2015**, *5*, 8335.

[39] Y. Yang, Q. Sun, Y.-S. Li, H. Li, Z.-W. Fu, *J. Power Sources* **2013**, *223*, 312.

[40] R. Gao, J. Zhu, X. Xiao, Z. Hu, J. Liu, X. Liu, *J. Phys. Chem. C* **2015**, *119*, 4516.

[41] W.-H. Ryu, T.-H. Yoon, S. H. Song, S. Jeon, Y.-J. Park, I.-D. Kim, *Nano Lett.* **2013**, *13*, 4190.

[42] Y. Cui, Z. Wen, Y. Liu, *Energy Environ. Sci.* **2011**, *4*, 4727.

[43] R. Black, J.-H. Lee, B. Adams, C. A. Mims, L. F. Nazar, *Angew. Chem.* **2013**, *52*, 392.

[44] L. Li, S. Liu, A. Manthiram, *Nano Energy* **2015**, *12*, 852.

[45] Y. Zhao, L. Xu, L. Mai, C. Han, Q. An, X. Xu, X. Liu, Q. Zhang, *Proc. Natl. Acad. Sci. USA* **2012**, *109*, 19569.

[46] S. C. Riha, B. M. Klahr, E. C. Tyo, S. Seifert, S. Vajda, M. J. Pellin, T. W. Hamann, A. B. F. Martinson, *ACS Nano* **2013**, *7*, 2396.

[47] B. Huang, W. Yang, Y. Wen, B. Shan, R. Chen, *ACS Appl. Mater. Interfaces* **2014**, *7*, 422.

[48] M. E. Donders, H. C. M. Knoops, M. C. M. van de Sanden, W. M. M. Kessels, P. H. L. Notten, *J. Electrochem. Soc.* **2011**, *158*, G92.

[49] K. B. Klepper, O. Nilsen, H. Fjellvag, *J. Cryst. Growth* **2007**, *307*, 457.

[50] M. Rooth, E. Lindahl, A. Hårsta, *Chem. Vap. Deposition* **2006**, *12*, 209.

[51] K. B. Klepper, O. Nilsen, H. Fjellvåg, *Thin Solid Films* **2007**, *515*, 7772.

[52] M. E. Donders, H. C. M. Knoops, W. M. M. Kessels, P. H. L. Notten, *J. Power Sources* **2012**, *203*, 72.

[53] X. Xia, Z. Zeng, X. Li, Y. Zhang, J. Tu, N. C. Fan, H. Zhang, H. J. Fan, *Nanoscale* **2013**, *5*, 6040.

[54] Q. Sun, H. Yadegari, M. N. Banis, J. Liu, B. Xiao, X. Li, C. Langford, R. Li, X. Sun, *J. Phys. Chem. C* **2015**, *119*, 13433.

[55] N. Zhao, X. Guo, *J. Phys. Chem. C* **2015**, *119*, 25319.

[56] W.-J. Kwak, Z. Chen, C. S. Yoon, J.-K. Lee, K. Amine, Y.-K. Sun, *Nano Energy* **2015**, *12*, 123.

[57] N. Ortiz-Vitoriano, T. P. Batcho, D. G. Kwabi, B. Han, N. Pour, K. P. C. Yao, C. V. Thompson, Y. Shao-Horn, *J. Phys. Chem. Lett.* **2015**, *6*, 2636.

[58] C. Xia, R. Black, R. Fernandes, B. Adams, L. F. Nazar, *Nat. Chem.* **2015**, *7*, 496.

[59] N. Zhao, C. Li, X. Guo, *Phys. Chem. Chem. Phys.* **2014**, *16*, 15646.

[60] J. M. García, H. W. Horn, J. E. Rice, *J. Phys. Chem. Lett.* **2015**, *6*, 1795.

[61] N. Kumar, M. D. Radin, B. C. Wood, T. Ogitsu, D. J. Siegel, *J. Phys. Chem. C* **2015**, *119*, 9050.

[62] R. S. Assary, K. C. Lau, K. Amine, Y.-K. Sun, L. A. Curtiss, *J. Phys. Chem. C* **2013**, *117*, 8041.

[63] Y. Shao, F. Ding, J. Xiao, J. Zhang, W. Xu, S. Park, J.-G. Zhang, Y. Wang, J. Liu, *Adv. Funct. Mater.* **2013**, *23*, 987.

[64] M. Balaish, A. Kraytsberg, Y. Ein-Eli, *Phys. Chem. Chem. Phys.* **2014**, *16*, 2801.

[65] J. Lu, L. Li, J.-B. Park, Y.-K. Sun, F. Wu, K. Amine, *Chem. Rev.* **2014**, *114*, 5611.

[66] D. Sharon, D. Hirshberg, M. Afri, A. Garsuch, A. A. Frimer, D. Aurbach, *Isr. J. Chem.* **2015**, *55*, 508.

[67] D. Geng, N. Ding, T. S. A. Hor, S. W. Chien, Z. Liu, D. Wuu, X. Sun, Y. Zong, *Adv. Energy Mater.* **2016**, *6*, 1502164.

[68] N. Feng, P. He, H. Zhou, *Adv. Energy Mater.* **2016**, *6*, 1502103.

[69] X. Yao, Q. Dong, Q. Cheng, D. Wang, *Angew. Chem. Int. Ed.* **2016**, *55*, 11344.

[70] Y. Li, X. Wang, S. Dong, X. Chen, G. Cui, *Adv. Energy Mater.* **2016**, *6*, 1600751.

[71] S. A. Freunberger, Y. Chen, N. E. Drewett, L. J. Hardwick, F. Bardé, P. G. Bruce, *Angew. Chem. Int. Ed.* **2011**, *50*, 8609.

[72] R. Black, A. Shyamsunder, P. Adeli, D. Kundu, G. K. Murphy, L. F. Nazar, *ChemSusChem* **2016**, *9*, 1795.

[73] E. N. Nasybulin, X. Wu, B. L. Mehdi, E. Thomsen, M. H. Engelhard, R. C. Masse, P. Bhattacharya, M. Gu, W. Bennett, Z. Nie, C. Wang, N. D. Browning, J. Zhang, *ACS Appl. Mater. Interfaces*, **2014**, *6*, 14141.

[74] B. D. McCloskey, J. M. Garcia, A. C. Luntz, *J. Phys. Chem. Lett.* **2014**, *5*, 1230.

[75] R. Manigandan, K. Giribabu, R. Suresh, V. Narayanan, A. Stephen, L. Vijayalakshmi, *Chem. Sci. Trans.* **2013**, *2*, S47.

[76] M. H. Brooker, J. B. Bates, *J. Chem. Phys.* **1971**, *54*, 4788.

[77] A. Moen, D. G. Nicholson, B. S. Clausen, P. L. Hansen, A. Molenbroek, G. Steffensen, *Chem. Mater.* **1997**, *9*, 1241.

[78] F. Morales, D. Grandjean, A. Mens, F. M. F. de Groot, B. M. Weckhuysen, *J. Phys. Chem. B* **2006**, *110*, 8626.

[79] B.-M. Chae, E.-S. Oh, Y.-K. Lee, *J. Power Sources* **2015**, *274*, 748.

[80] K. P. C. Yao, M. Risch, S. Y. Sayed, Y.-L. Lee, J. R. Harding, A. Grimaud, N. Pour, Z. Xu, J. Zhou, A. Mansour, F. Barde, Y. Shao-Horn, *Energy Environ. Sci.* **2015**, *8*, 2417.

ADVANCED
FUNCTIONAL
MATERIALS
www.afm-journal.de

ADVANCED
SCIENCE NEWS
www.advancedsciencenews.com

FULL PAPER

[81] G. P. Huffman, N. Shah, J. M. Zhao, F. E. Huggins, T. E. Hoost, S. Halvorsen, J. G. Goodwin, *J. Catal.* **1995**, *151*, 17.

[82] Y. Wang, C. Zhang, F. Liu, H. He, *Appl. Catal., B: Environ.* **2013**, *142–143*, 72.

[83] N. Koizumi, S. Suzuki, Y. Ibi, Y. Hayasaka, Y. Hamabe, T. Shindo, M. Yamada, *J. Synchrotron Radiat.* **2012**, *19*, 74.

[84] J. Zhong, H. Zhang, X. Sun, S.-T. Lee, *Adv. Mater.* **2014**, *26*, 7786.

[85] F. M. F. de Groot, E. de Smit, M. M. van Schooneveld, L. R. Aramburo, B. M. Weckhuysen, *ChemPhysChem* **2010**, *11*, 951.

[86] J. Zhou, J. Wang, H. Liu, M. N. Banis, X. Sun, T.-K. Sham, *J. Phys. Chem. Lett.* **2010**, *1*, 1709.

[87] J. Wang, J. Zhou, Y. Hu, T. Regier, *Energy Environ. Sci.* **2013**, *6*, 926.

[88] X. Chen, J. Xiao, J. Wang, D. Deng, Y. Hu, J. Zhou, L. Yu, T. Heine, X. Pan, X. Bao, *Chem. Sci.* **2015**, *6*, 3262.

[89] H. Yadegari, M. N. Banis, B. Xiao, Q. Sun, X. Li, A. Lushington, B. Wang, R. Li, T.-K. Sham, X. Cui, X. Sun, *Chem. Mater.* **2015**, *27*, 3040.

[90] M. D. Radin, C. W. Monroe, D. J. Siegel, *Chem. Mater.* **2014**, *27*, 839.

[91] P. Hartmann, M. Heinemann, C. L. Bender, K. Graf, R.-P. Baumann, P. Adelhelm, C. Heiliger, J. Janek, *J. Phys. Chem. C* **2015**, *119*, 22778.

[92] B. Lee, J. Kim, G. Yoon, H.-D. Lim, I.-S. Choi, K. Kang, *Chem. Mater.* **2015**, *27*, 8406.

[93] J. Kim, H. Park, B. Lee, W. M. Seong, H.-D. Lim, Y. Bae, H. Kim, W. K. Kim, K. H. Ryu, K. Kang, *Nat. Commun.* **2016**, *7*, 10670.

[94] Y. Chen, S. A. Freunberger, Z. Peng, O. Fontaine, P. G. Bruce, *Nat. Chem.* **2013**, *5*, 489.

[95] M. Yu, X. Ren, L. Ma, Y. Wu, *Nat. Commun.* **2014**, *5*, 5111.

[96] D. Sun, Y. Shen, W. Zhang, L. Yu, Z. Yi, W. Yin, D. Wang, Y. Huang, J. Wang, D. Wang, J. B. Goodenough, *J. Am. Chem. Soc.* **2014**, *136*, 8941.

[97] B. J. Bergner, A. Schürmann, K. Peppler, A. Garsuch, J. Janek, *J. Am. Chem. Soc.* **2014**, *136*, 15054.

[98] D. Su, S. Dou, G. Wang, *Sci. Rep.* **2014**, *4*, 5767.

[99] W. Fan, X. Guo, D. Xiao, L. Gu, *J. Phys. Chem. C* **2014**, *118*, 7344.

[100] M. Hong, H. C. Choi, H. R. Byon, *Chem. Mater.* **2015**, *27*, 2234.

[101] J. Zhou, J. Wang, H. Fang, T.-K. Sham, *J. Mater. Chem.* **2011**, *21*, 5944.

[102] J. Wang, J. Zhou, H. Fang, T.-K. Sham, C. Karunakaran, Y. Lu, G. Cooper, A. P. Hitchcock, *J. Electron Spectrosc. Relat. Phenom.* **2011**, *184*, 296.

[103] J. Zhou, J. Wang, Y. Hu, T. Regier, H. Wang, Y. Yang, Y. Cui, H. Dai, *Chem. Commun.* **2013**, *49*, 1765.

[104] C. Zhou, J. Wang, J. A. Szpunar, *Chem. Commun.* **2014**, *50*, 2282.

[105] J. Zhou, J. Wang, J. Cutler, E. Hu, X.-Q. Yang, *Phys. Chem. Chem. Phys.* **2016**, *18*, 22789.